Validation of formaldehyde products from three satellite retrievals (OMI SAO, OMPS-NPP SAO, and OMI BIRA) in the marine atmosphere with four seasons of ATom aircraft observations

Jin Liao[1,2], Glenn M. Wolfe[1], Alexander E. Kotsakis[1,3,*], Julie M. Nicely[1,4], Jason M. St. Clair[1,2], Thomas F. Hanisco[1], Gonzalo González Abad[5], Caroline R. Nowlan[5], Zolal Ayazpour[5,6], Isabelle De Smedt[7], Eric C. Apel[8], Rebecca S. Hornbrook[8]

[1]Atmospheric Chemistry and Dynamic Laboratory, NASA Goddard Space Flight Center, Greenbelt, MD, USA
[2]Goddard Earth Sciences Technology and Research (GESTAR II), University of Maryland, Baltimore County, MD, USA
[3]Earth Resources Technology (ERT) Inc., Laurel, MD, USA
[4]Earth System Science Interdisciplinary Center (ESSIC), University of Maryland, College Park, MD, USA
[5]Center for Astrophysics Harvard-Smithsonian, Cambridge, MA, USA
[6]Department of Civil, Structural and Environmental Engineering, University of Buffalo, Buffalo, NY, USA
[7]Royal Belgian Institute for Space Aeronomy (BIRA-IASB), Brussels, Belgium
[8]Atmospheric Chemistry Observations & Modeling Laboratory, National Center for Atmospheric Research (NCAR), Boulder, CO, USA
[*]Now at Earth System Science Interdisciplinary Center (ESSIC), University of Maryland, College Park, MD, USA

Correspondence to: Jin Liao (jin.liao@nasa.gov)

Abstract. Formaldehyde (HCHO) in the atmosphere is an intermediate product from the oxidation of methane and non-methane volatile organic compounds. In remote marine regions, HCHO variability is closely related to atmospheric oxidation capacity and modeled HCHO in these regions is usually added as a global satellite HCHO background. Thus, it is important to understand and validate the levels of satellite HCHO over the remote oceans. Here we intercompare three satellite retrievals of total HCHO columns (OMI-SAO (v004), OMPS-NPP SAO, and OMI BIRA) and validate them against in situ observations from the NASA Atmospheric Tomography Mission (ATom) mission. All retrievals are correlated with ATom integrated columns over remote oceans, with OMI SAO (v004) showing the best agreement. This is also reflected in the mean bias (MB) for OMI SAO (-0.73±0.87) $\times$ 10^{15} molec cm^{-2}, OMPS SAO (-0.76±0.88) $\times$ 10^{15} molec cm^{-2}, and OMI BIRA (-1.40±1.11) $\times$ 10^{15} molec cm^{-2}. We recommend the OMI-SAO (v004) retrieval for remote ocean atmosphere studies. Three satellite HCHO retrievals and in situ ATom columns all generally captured the spatial and seasonal distributions of HCHO in the remote ocean atmosphere. Retrieval bias varies by latitude and season, but a persistent low bias is found in all products at high latitudes and the general low bias is most severe for the OMI BIRA product. Examination of retrieval components reveals slant column corrections have a larger impact on the retrievals over remote marine regions

34 while AMFs play a smaller role. This study informs that the potential latitude-dependent biases in the retrievals require further investigation for

35 improvement and should be considered when using marine HCHO satellite data, and vertical profiles from in situ instruments are crucial for

36 validating satellite retrievals.

37

38

1 Introduction

Formaldehyde (HCHO) in the marine atmosphere is mainly produced from oxidation of methane. Non-methane volatile organic compounds (VOCs) transported from continents and potentially VOCs emitted at the ocean surface (Guenther et al., 1995; Novak and Bertram, 2020) may also contribute to the marine HCHO. Methane is the dominant precursor of HCHO in the remote atmosphere and oxidation of methane by hydroxyl radical (OH) represents ~ 80% of the global HCHO source (Fortems-Cheiney et al., 2012; Wolfe et al., 2019). Satellite HCHO columns have been used to estimate the levels of atmospheric oxidant OH, which plays an important role in removing air pollutants and greenhouse gas methane (Wolfe et al., 2019). HCHO in the clean remote ocean atmosphere is considered as HCHO tropospheric background due to the short atmospheric lifetime of HCHO of a few hours and its source locations. The column abundance of HCHO ranges from $\sim 1 \times 10^{15}$ molec cm^{-2} in the remote troposphere (Vigouroux et al., 2018; Zhu et al., 2020) to the order of 10^{16} molec cm^{-2} over continental regions (Zhu et al., 2016).

HCHO is one of the few VOCs that can be observed from space. Satellite HCHO observations have been obtained by Global Ozone Monitoring Experiment (GOME) (1995-2011) (Chance et al., 2000; Thomas et al., 1998), the Scanning Imaging Absorption SpectroMeter for Atmospheric ChartographY (SCIAMACHY) (2002–2012) (De Smedt et al., 2008), GOME-2 (2006–2021/2012–present/2018–present) (De Smedt et al., 2012), the Ozone Monitoring Instrument (OMI) (2004–present) (De Smedt et al., 2015; González Abad et al., 2015), the Ozone Mapping and Profiler Suite (OMPS) on Suomi NPP (Li et al., 2015; González Abad et al., 2016; Nowlan et al., 2023) and on NOAA-20 (2017–present) (Nowlan et al., 2023), and the TROPOspheric Monitoring Instrument (Sentinel-5P/TROPOMI) (2017–present) (De Smedt et al., 2021, 2018). Geostationary satellite instruments also retrieve HCHO, including the Geostationary Environment Monitoring Spectrometer (GEMS) (Kim et al., 2020; Kwon et al., 2019) over East Asia (2020–present), Tropospheric Emissions: Monitoring of Pollution (TEMPO) (Chance et al., 2019) over North America (2023–present) and the upcoming European Sentinel-4 mission (Gulde et al., 2017). Major retrieval algorithms for HCHO include those developed by the Smithsonian Astrophysical Observatory (SAO), Belgian Institute for Space Aeronomy (BIRA), and NASA Goddard Space Flight Center (GSFC). These algorithms have evolved over time.

Previous studies have validated satellite HCHO retrievals with airborne and ground-based in situ and remote sensing instruments in different settings and contexts. Zhu et al. (2016) indirectly evaluated six retrievals from four sensors against airborne observations in the isoprene-rich Southeast U.S. using a model as an intermediary, finding a low bias in the mean by 20–51% for all retrievals. Zhu et al. (2020) extend this method to indirectly validate OMI SAO v003 data with in-situ HCHO measurements from 12 aircraft campaigns over North America, East Asia, and the remote Pacific Ocean. They found that the OMI SAO v003 product has negative biases (-44:5% to -21:7%) under high-HCHO conditions and high biases (+66:1% to +112:1 %) under low-HCHO conditions (Zhu et al., 2020). De Smedt et al. (2021) validated TROPOMI and OMI-

BIRA HCHO against a Multi-axis differential optical absorption spectroscopy (MAX-DOAS) ground network, finding that compared to the MAX-DOAS ground network, TROPOMI HCHO columns are biased low especially for high concentrations and OMI-BIRA HCHO columns are biased high at low concentrations and biased low at high concentrations (De Smedt et al., 2021). In validation using Fourier transform infrared (FTIR) data, TROPOMI HCHO columns were biased high for low concentrations sites and biased low for high concentrations sites and the correlation between TROPOMI and FTIR HCHO columns yields a slope of 0.64 and an intercept of 1.10×10^{15} molecules cm^{-2} (Vigouroux et al., 2020). OMPS Suomi NPP and NOAA-20 HCHO columns generally have good agreement with NDACC FTIR observations at 24 sites. The linear regression between OMPS-NPP and FTIR HCHO columns yields a slope of 0.82 and an intercept of 5.71×10^{14} molecules cm^{-2} and the linear regression between OMPS-NOAA20 and FTIR reveals a slope of 0.92 and an intercept of 6.76×10^{14} molecules cm^{-2} (Kwon et al., 2023). OMPS-NPP and OMPS-NOAA20 HCHO columns are also biased high compared to FTIR measurements for sites with low HCHO levels (Kwon et al., 2023).

Most validation efforts focus on continental regions, while comparatively few examine the remote marine atmosphere. No previous validation of satellite HCHO over the remote oceans with airborne in situ measurement was performed before the NASA ATom field campaigns (2016–2018). OMI SAO v003 retrieval has been compared to two seasons of ATom observations over both Pacific and Atlantic Oceans (Wolfe et al., 2019) and over the clean Pacific Ocean (Zhu et al., 2020), with HCHO columns ranging from 1×10^{15} to 8×10^{15} molecules cm^{-2}. The ground FTIR HCHO measurements at Mauna Loa in the Pacific Ocean domain are about 1×10^{15} molecules cm^{-2} for the background atmosphere measurements (Vigouroux et al., 2018).

The accuracy of model predicted HCHO over the Pacific Ocean affects the global HCHO background in satellite retrievals. In satellite HCHO retrievals, differential HCHO slant columns are often derived using spectra measured over a reference sector in the Pacific Ocean, and modeled HCHO columns over the reference sector are added back to account for the real HCHO levels over the reference sector (De Smedt et al., 2018; Nowlan et al., 2023). The locations of the area in the Pacific Ocean used as reference sectors vary among different retrievals (De Smedt et al., 2018; Nowlan et al., 2023). Modeled HCHO levels over the remote Pacific Ocean also play a role in correcting some biases such as latitude-dependent biases in slant columns (De Smedt et al., 2018; Nowlan et al., 2023). Consequently, quantitative assessment of satellite HCHO over the remote ocean is crucial for assessing the satellite's ability to accurately capture background HCHO levels and deepening our understanding of these baseline levels. Refining satellite HCHO retrievals will reduce potential bias in applications such as estimating VOC emissions and atmospheric oxidant levels.

103 Here we present a systematic comparison of in situ HCHO columns from four seasons of ATom observations with three commonly-used satellite

104 retrievals. Study objectives include 1) quantify spatial and seasonal retrieval bias, 2) quantify differences between retrievals, and 3) identify

105 relative contributions of retrieval components to inter-retrieval differences and overall bias.

106

107 **2. Methods**

108 **2.1 ATom observations**

109 The NASA ATom mission studied atmospheric composition from near pole-to-pole over the Pacific and Atlantic remote oceans with frequent

110 vertical profiling from above the sea surface (100 m) to 10-12 km altitude for four seasons during 2016-2018 (Thompson et al., 2022).

111

112 The primary source of in situ HCHO measurements for this study is the In Situ Airborne Formaldehyde (ISAF) instrument (Cazorla et al., 2015).

113 ISAF data are reported at 1 Hz with a 1σ precision of 30 pptv. Systematic uncertainty is estimated as 10% + 10 pptv based on pre- and post-

114 mission calibration against compressed gas standards. ISAF measurements are not available during the second half of ATom 4, thus we also use

115 HCHO observations from the Trace Organic Gas Analyzer (TOGA) instrument (Apel et al., 2003, 2015). The TOGA reporting period is 2

116 minutes, and reported HCHO accuracy is 40% $\pm$ 40 pptv. Brune et al. (2020) performed a comparison of ISAF and TOGA data for all four ATom

117 deployments and found mission-to-mission variability in measurement agreement, with relatively good agreement for ATom-4. Similarly, we find

118 that the two measurements agree well for this deployment (Figure S1, slope of 1.1). Due to the higher accuracy and measurement frequency of

119 ISAF than TOGA, ISAF HCHO measurements from ATom are used when available.

120

121 ATom in situ HCHO composite columns are derived from the ATom vertical profiles. Ascents and descents occur along transits between

122 locations and typically cover 200-450 km in horizontal distance (Wolfe et al., 2019). In situ HCHO columns are compared to the average of

123 satellite grid cells intersected by the in situ profile area and calculated using the method described in Wolfe et al. (2019). Each profile is averaged

124 to an altitude grid of 0 to 10 km with 200 m spacing. Few measurements above 10 km are excluded. The lowest (or highest) altitude

125 measurements are extrapolated to the surface 0 km or (10 km) using the average of the two lowest (or highest) altitude measurements of that

126 profile. Missing data in between are linearly interpolated. Columns are filtered to include only profiles with solar zenith angle smaller than 80°,

127 minimum altitude <= 600 m, maximum altitude >= 8 km, fraction of missing measured data in the altitude profiles < 0.2, and fraction of missing

128 extrapolated data between 0 to 10 km <0.25. The average missing interpolated data within 0 – 10 km is 8%, mostly due to lower resolution

129 TOGA data are used during ATOM 4. The data gaps are typically small and lack significant structure, so we expect them to contribute to random

| Deleted: fraction of interpolated grids |
| Deleted: extrapolation |

132 error rather than introduce any systematic bias. The average missing extrapolated data between 0 – 10 km is 5%. Most HCHO > 10 km were not

133 measured during ATom field campaign so modeled results, average gas profiles from OMI SAO HCHO retrievals, are used to estimate the

134 contribution of HCHO above 10 km to the total HCHO column. The gas profiles in OMI SAO retrieval are from GEOS-Chem 2018 monthly

135 climatology 0.5º×0.5º (Table 1). The fraction of HCHO above 10 km (relative to the total column) is 0.045± 0.002, calculated by integrated gas

136 profiles above 10 km divided by the integrated gas profiles from 0- 40 km. This value is used to scale up in situ HCHO columns for comparison

137 with satellite retrievals.

138

139 **2.2 Satellite HCHO retrieval products**

140 **2.2.1 OMI SAO (v004)**

141 OMI was launched in 2004 onboard the NASA Aura satellite. It has a native spatial resolution at nadir of 24×13 km^2 (Table 1) with daily global

142 coverage at a local overpass time of 13:30. The Smithsonian Astrophysical Observatory (SAO) version 004 retrieval is the updated version of

143 OMI SAO v003 (González Abad et al., 2015) and is identical to the OMPS-NPP SAO retrieval (Nowlan et al., 2023). The algorithm involves two

144 main steps: 1) Following line shape and spectral calibration, spectral fitting at 328.5-356.5 nm range for individual ground pixel is applied and a

145 reference spectrum from a clean region over the Pacific Ocean is used with the measured spectrum to derive the differential slant column

146 (ΔSCD), and 2) converting the resultant ΔSCD to vertical column density (VCD) using slant column corrections and the air mass factor (AMF).

147 The HCHO absorption cross section used in OMI SAO 004 is from Chance and Orphal (2011) at 300 K (Table 1). The location of the reference

148 spectrum is over the clean Pacific Ocean but varies slightly day-to-day due to orbit overpass location. The OMI SAO reference spectrum at each

149 across-track position is determined by averaging all spectra collected at that position between latitudes 30° S and 30° N from the orbit closest in

150 time and with an equatorial crossing closest to 160° W and within 140° W and 180° W (Nowlan et al., 2023). The spectra at the reference locations

151 are also used for slant column reference sector corrections including HCHO background addition as described below.

152

153 The ΔSCD is converted to VCD through Eq. (1).

154

155 $VCD = (\Delta SCD + SCD_{Ref} + SCD_B)/AMF$, (1)

156

157 Where SCD_{Ref} is reference sector correction; SCD_B is bias correction; and $\Delta SCD + SCD_{Ref} + SCD_B$ is also referred to as the corrected slant

158 column. The SCD_{Ref} corrects the cross-track pixel dependence sensitivity and adds HCHO background slant columns from the reference region

163 from a chemical transport model (VCD from CTM model×AMF) (Nowlan et al., 2023). The SCD_B is from the modeled columns of HCHO and

164 used to correct what are primarily latitude-dependent biases in the retrieved ΔSCD, likely due to interfering absorbers and insufficiently corrected

165 instrument calibration issues (Nowlan et al., 2023).

166

167 The AMF defines the mean photon path across the atmosphere and is used in the retrievals to convert slant columns into vertical columns (Eq.

168 (1)). AMF is calculated by the product of altitude-dependent gas phase HCHO shape factors (S) and scattering weights (w) integrated along the

169 vertical coordinate (Eq. (2)). Shape factor (S) is the normalized HCHO vertical number density and calculated from the product of altitude

170 dependent HCHO mixing ratio C and air mass density M normalized by HCHO column density (see Eq. (3)). The HCHO vertical mixing ratio

171 profile (or *a priori* profile) comes from a GEOS-Chem 2018 monthly climatology at 0.5º × 0.5º resolution. Scattering weights are altitude-

172 dependent HCHO measurement sensitivities and are calculated from a vector multiple-scatter multilayer discrete-ordinate radiative transfer model

173 (VLIDORT) v2.8 (Spurr, 2006). Scattering weights depend on the viewing angles, surface albedo, surface pressure and clouds. The scattering

174 and absorption of abnormal aerosol loading can also affect scattering weights and may not be properly represented in calculated scattering

175 weights (e.g., unpredicted biomass burning plumes).

176 $\text{AMF} = \int_0^z w(z)S(z)dz$,   (2)

177 $S(z) = \dfrac{C(z)M(z)}{\int_0^z C(z)M(z)dz}$,   (3)

178

179 Previous comparisons of airborne to satellite HCHO data used OMI SAO v003 (Wolfe et al., 2019; Zhu et al., 2020). OMI SAO v003 retrieves

180 slant column density using direct differential optical absorption spectroscopy (DOAS) (Gonzalez Aabd et al., 2015). To show the difference between

181 OMI SAO v004 and OMI SAO v003, the global maps of HCHO from OMI SAO v004, OMI SAO v003 and their difference with the temporal

182 average for the ATom-1 time period are provided in supplementary Figure S2.

183 **2.2.2 OMPS-NPP SAO**

184 OMPS is onboard the joint NASA/NOAA Suomi National Polar-orbiting Partnership (NPP) satellite that was launched in 2011 with a spatial

185 resolution at nadir of 50 × 50 km and daily global coverage. OMPS also has an equatorial crossing time of about 13:30 local time. The retrieval of

186 OMPS-SAO is described in Nowlan et al., (2023), and is identical to that described above (Sect. 2.1.1). The spatial and temporal coverage of

187 OMPS and OMI differ due to both their native spatial resolutions and the OMI row anomaly (González Abad et al., 2016).

2.2.3. OMI BIRA

OMI BIRA is the European Union Quality Assurance for Essential Climate Variables (QA4ECV) product (De Smedt et al., 2015; Zara et al., 2018). It is basically the same retrieval algorithm as the operational product of TROPOspheric Monitoring Instrument (TROPOMI) launched in October 2017 (De Smedt et al., 2021). The detailed retrieval algorithms are described in De Smedt et al. (2018) and only a brief description is provided here. OMI BIRA retrieval also involves two steps. The spectra fitting window is 328.5–359 nm, slightly larger than SAO retrievals. For OMI BIRA, slant column densities are converted to vertical columns as Eq. (5).

$$VCD = (\Delta SCD - N_{s,0})/AMF + N_{v,0} , \hspace{4cm} (5)$$

$N_{s,0}$, the slant column correction, corrects the remaining global offset and possible stripes (cross-track pixel dependence sensitivity) of the differential slant column. $N_{v,0}$, the vertical column correction, is from the TM5 model to compensate for a background HCHO level due to methane oxidation in the equatorial Pacific (De Smedt et al., 2021). The corrected slant column is defined as differential slant column (ΔSCD) minus slant column correction ($N_{s,0}$) plus the product of vertical column correction ($N_{v,0}$) and AMF. The OMI BIRA gas profile comes from TM5-MP model $1^{\circ} \times 1^{\circ}$ daily data. The radiative transfer model for OMI BIRA is VLIDORT v2.7 (De Smedt et al., 2017) , a slightly different version from that used in the SAO retrievals. In the OMI BIRA retrieval, the location of reference sector for destriping and global offset correction is between latitudes 5°S and 5°N and longitudes 120°W and 180°W and for zonal correction is between latitudes 90°S and 90°N and longitudes 120°W and 180°W (De Smedt et al., 2017). Considering the locations of the reference sectors (see Figure S3), understanding of the HCHO concentration over the clean Pacific Ocean is important for evaluating the accuracy of satellite HCHO retrievals.

Table 1. Parameters in satellite retrievals

	Nadir pixel resolution (km²)	Fitting windows (nm)	HCHO absorption cross section	Chemical Transport Model (CTM)	Radiative transfer model and wavelength for calculation	Trace gas profiles	Reference sector locations
OMI SAO	24 × 13	328.5-356.5	HITRAN (Chance and Orphal, 2011), 300 K	GEOS-Chem v09-01-03	VLIDORT v2.8, 340 nm	GEOS-Chem 2018 monthly climatology 0.5°×0.5°	Latitudes :30˚S - 30˚N longitudes: an equatorial crossing closest to 160˚W and between 140˚W and 180˚W
OMPS-NPP SAO	50 × 50	the same as above	the same as above	the same as above	the same as above	the same as above	the same as above
OMI BIRA	24 × 13	328.5-359	Meller and Moortgat, 2000, 298K	TM5-MP	VLIDORT v2.7, 340 nm	TM5-MP daily profiles, 1°×1°	Destripping and global offset correction: latitudes 5˚S–5˚N, longitudes 120˚W–180˚W; Zonal correction: latitudes 90˚S–90˚N, longitudes 120˚W–180˚W

206

2.2.4 Retrieval uncertainties

Uncertainties in satellite retrievals come from instrument calibrations, slant column fitting processes, slant column corrections, and AMF calculations. Averaging damps random uncertainties, while the systematic uncertainties remain (Nowlan et al., 2023). Instrument noise, choice of fitting windows, HCHO cross-section error, surface reflectance, *a priori* profiles, vertical distribution and properties of clouds and aerosols all can contribute to the overall systematic uncertainties of satellite HCHO products. In the OMPS SAO retrieval, the systematic uncertainty in corrected slant column is about 20% (Nowlan et al., 2023). The error from surface reflectance is about 5% over water, from aerosols is about 0.3% in global mean (but considerably larger in polluted regions and individual observations), from profile shape is 5% at low HCHO concentrations, from cloud fraction is 1% and from cloud pressure is 5-15% (Nowlan et al., 2023). The total systematic error is about 26%. We assume other retrievals have similar or smaller systematic errors, as OMPS SAO uses climatological cloud pressure and probably has the largest uncertainty (Nowlan et al., 2023).

2.2.5 Satellite data filtering and gridding

OMI SAO and OMPS SAO HCHO data use the same categories to filter the data while OMI BIRA use slightly different filtering categories. SAO L2 data with solar zenith angle > 60°, cloud fraction > 40%, main data quality flag not equal to 0 are excluded. OMI BIRA L2 data with solar zenith angle > 60°, cloud fraction > 40%, and processing error flag $\neq 0$ but ≤ 255 are excluded.

The 3-D data such as gas profiles are first re-gridded to a universal vertical grid coordinate for all pixels. The L2 2-D and 3-D data are then gridded into 0.5° × 0.5° using an area weighted average (e.g, AMF, Gas Profiles), shown in Eq. (6), or uncertainty weighted average (e.g., HCHO column density), as shown in Eq. (7).

$$\overline{C_{ai}} = \frac{\sum_n C_n A_{n,i}}{\sum_n A_{n,i}}, \tag{6}$$

$$\overline{C_i} = \frac{\sum_n \frac{C_n A_{n,i}}{A_n E_n^2}}{\sum_n \frac{A_{n,i}}{A_n E_n^2}}, \tag{7}$$

229 where is $\overline{C_{ai}}$ is the area weighted average value (such as AMF) for grid i, $\overline{C_i}$ is the uncertainty weighted average value (such as HCHO column

230 density) for grid i, C_n is the HCHO column density for pixel n, $A_{n,i}$ is the area contribution of pixel n to grid i, A_n is the total area of pixel n, and

231 E_n is the uncertainty of HCHO column density for pixel n.

232

233 The gridded $0.5° \times 0.5°$ daily satellite HCHO data are averaged over each ATom period (ATom-1: 29 July – 23 August, 2016; ATom-2: 26

234 January – 21 February, 2017; ATom-3: 28 September – 27 October, 2017; ATom-4: 24 April – 21 May, 2018). Differential slant column, slant

235 column corrected, and vertical column all use uncertainty weighted averaging (Eq. (6)). For comparison to in situ HCHO composite columns, the

236 latitude and longitude coverage of the in situ profile are identified and the satellite HCHO grids intercepted with the profile latitudes and

237 longitudes are averaged to compare to the calculated in situ HCHO composite column.

238 **3. Results and discussions**

239 **3.1 Global distribution and seasonal variability of HCHO in the marine atmosphere**

240 Global HCHO distributions from all three retrievals and in situ composite columns across the Pacific and Atlantic Oceans show enhancement in

241 the tropics and decrease toward polar regions (Figures 1 and 2). The HCHO vertical column density over the remote ocean atmosphere ranges

242 from about 4×10^{15} molecules cm^{-2} at low latitudes to about 1×10^{15} molecules cm^{-2} at high latitudes. These large-scale features reflect similar

243 latitudinal and seasonal variability in OH and photolysis rates. Although the random noise for satellite HCHO such as OMPS SAO is about 3.5

244 $\times10^{15}$ molecules cm^{-2} (Nowlan et al., 2023), averaging in time and space largely reduces the noise and thus the variability of HCHO in the remote

245 ocean atmosphere can be well captured with near one-month average data. In situ HCHO columns corroborate the latitudinal-dependent HCHO

246 trend over the remote oceans.

Deleted: 3

Deleted: 3

Deleted: 3
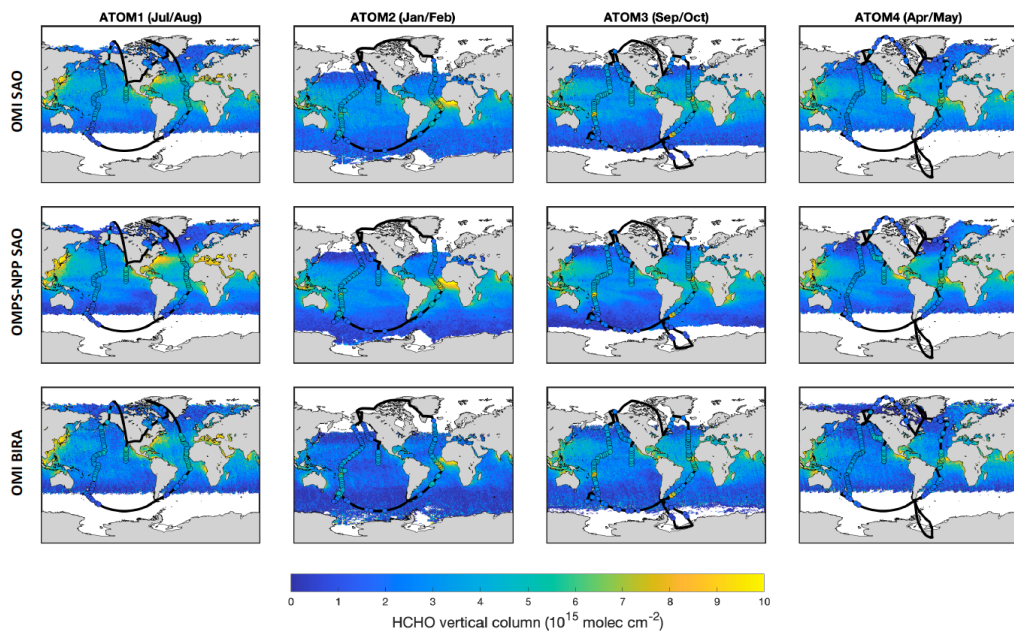
250
251 **Figure 1. Maps of HCHO vertical column density from three satellite retrievals (OMI-SAO, OMPS-SAO and OMI-BIRA, top to bottom) over the**
252 **oceans during four ATom measurement seasons (left to right) overlaid with in situ HCHO columns (colored dots) along the ATom flight tracks (black**
253 **lines). The color bar for both satellite and in situ HCHO composite columns is the same and saturates at both ends.**

254

255 Besides background methane oxidation, continental outflow also affects marine HCHO. All three satellite retrievals capture the continental

256 outflow of HCHO or its precursors from East Asia, North America, Africa, and South Asia (Figure 1). These enhancements can be significant; for

257 example, HCHO off the Atlantic coast of equatorial Africa in February reaches 1.1×10^{16} molecules cm^{-2}, sampled by ATom-2. ATom-3

258 observed enhanced HCHO in the vicinity of Fiji island when DC8 landed and took off (Figure 1). This enhancement is likely due to local

259 emissions and thus is excluded from the analysis below. Enhanced HCHO mixing ratios near Argentina is also observed during ATom-3. This

260 may be due to a transient biomass burning plume, as black carbon is also enhanced at this time, though carbon monoxide (CO) is not enhanced.

261 Satellite HCHO data also do not show a sustained enhancement at this location. The in situ HCHO composite column enhancement in ATom-3

262 near Argentina was also excluded from the following analysis.

263

264   Zonal mean HCHO varies with season (Figure 2). During ATom-1 in July and August (boreal summer), peak HCHO occurs in a broad band

265   between latitudes near 15-35° N. During ATom 2 in January and February (austral summer), the maximum HCHO latitude occurs near 5° S with

266   enhancement extending down to 45° S. Maximum HCHO latitudes for ATom-3 and -4 (spring/fall) are near the equator ($\pm5^\circ$). For ATom-3 and

267   ATom-4, HCHO is systematically higher in the Northern Hemisphere for comparable latitudes (e.g., 3×10^{15} molecules cm^{-2} at 50° N vs. $2 \times$

268   10^{15} molecules cm^{-2} at 50° S for ATom-3). This, along with the asymmetric summer maxima, suggests that HCHO precursors (e.g., methane and

269   other VOCs) are more concentrated in the Northern Hemisphere and impact the distribution of HCHO over the remote ocean. Increased NO$_x$ and

270   ozone can also promote formation of OH and thus HCHO.

Formatted: Font: 10 pt
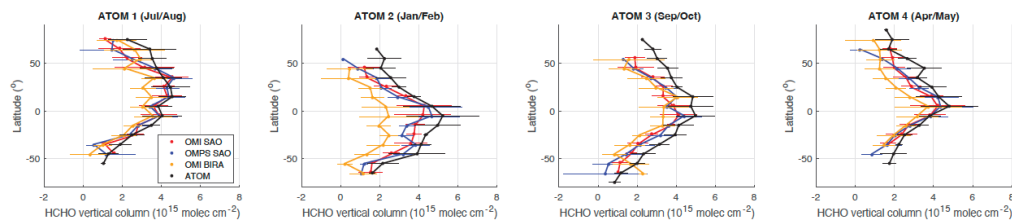
271
272   **Figure 2. HCHO column density from three satellite retrievals (OMI SAO in red, OMPS SAO in blue, and OMI BIRA in orange) and ATom in situ**
273   **measurements (black) at different latitudes. The dots represent the averaged column density for ± 5° latitude bins and the bars are the standard**
274   **deviation within the latitude bin. OMI SAO error bars are vertically offset for clarity.**
275

276   Continental outflows enhance HCHO near the coast, varying with seasons (Figure 1). Enhancements near East Asia, South Asia, North America

277   and Europe are highest during boreal summertime (ATom-1) and lowest during boreal winter time (ATom-2), reflecting higher biogenic

278   emissions and stronger photochemistry during the former. Biomass burning outflow from Africa also varied with seasons, peaking during ATom-

279   2 north of the equator and ATom-1 south of the equator. The biomass burning outflows from Africa impacted the ATom-2, -3 and -4 flights and

280   thus the Atlantic transits have higher HCHO concentrations than Pacific transits. The biomass burning impacted air masses are not excluded in

281   the analysis because the African biomass burning outflows affect large areas and likely happen yearly and can be considered as part of the

282   background.

283   **3.2 Comparison between retrievals and in situ HCHO columns**

284   Comparison of satellite HCHO with ATom in situ composite column densities provides validation of satellite HCHO over remote oceans,

285   assuming ATom sampling is representative of the monthly average conditions. All retrievals (OMI SAO, OMPS SAO and OMI BIRA) are well

286   correlated with in situ integrated columns ($r^2 \geq 0.74$), with slopes ranging from 0.75 to 1.33 for individual seasons and negative intercepts on the

287 order of 1×10^{15} molecules cm^{-2} (Figure 3; Table 2). The uncertainty in HCHO above 10 km is on the order of 10^{14} molecules cm^{-2} and cannot

288 account for the negative intercepts. Persistent negative intercepts may suggest a low bias or offset in all retrievals, maybe related to modeled

289 HCHO. GEOS-Chem predicted HCHO was higher than observed during TRACE-P (Singh et al., 2004) and in-between two HCHO observations

290 during INTEX-A (Millet et al., 2006). Considering all retrievals, OMI SAO exhibits the best agreement with ATom overall (slope = 1.02 ± 0.05,

291 intercept = $-0.8 \pm 0.2 \times 10^{15}$ molecules cm^{-2}). Considering individual ATom deployments, retrievals fall closest to the 1:1 line against ATom

292 columns for ATom1 (Figure 3). For ATom-2, OMI BIRA also appears to be systematically low with a slope of 0.75 ± 0.09. Low OMI BIRA

293 HCHO in ATom-2 is also evident in Figure 2. The mean bias of OMI SAO, OMPS SAO, and OMI BIRA HCHO column for all four

294 ATom is -0.73 ($\pm$0.87) $\times 10^{15}$ molec cm^{-2}, -0.76 ($\pm$0.88) $\times 10^{15}$ molec cm^{-2}, and -1.40 ($\pm$1.11) $\times 10^{15}$ molec cm^{-2}, respectively, listed

295 in Table 2. The mean bias matric also shows OMI SAO has the best agreement and OMI BIRA has the largest low bias with HCHO

296 vertical columns derived from in situ measurements.

297

298
299 **Figure 3. Scattered plots of satellite HCHO vertical columns from OMI SAO (a), OMPS SAO (b), and OMI BIRA (c) retrievals versus in situ integrated**
300 **vertical columns from four seasons: ATom-1 (red), ATom-2 (blue), ATom-3 (green) and ATom-4 (orange). Error bars for satellite data are the standard**
301 **deviation of the averaged grid cells, while error bars for in situ composite columns are propagated from the uncertainty of the in situ measurements:**
302 **$\pm$10% + 10 pptv (or ~4.8 $\times 10^{14}$ molec cm^{-2}) for ISAF and $\pm$40% (or 40 pptv, whichever is greater) (or ~ 1.9 $\times 10^{15}$ molecules cm^{-2}) for TOGA. The**
303 **colored lines and black line are the equally weighted linear regression for each ATom and the total ATom data, respectively. The 1: 1 line is shown as**
304 **the dashed line. The slopes and intercepts are summarized in Table 2. The higher standard deviations of OMI BIRA HCHO data are due to some large**
305 **negative values not filtered and do not imply large variation of OMI BIRA HCHO data.**

306
307 Table 2 Parameters for linear fits of satellite retrievals against ATom observations (see Figure 3).

	OMI SAO				OMPS SAO				OMI BIRA			
	Slope	Intercept ($\times 10^{15}$)	r^2	Mean Bias ($\times 10^{15}$)	Slope	Intercept ($\times 10^{15}$)	r^2	Mean Bias ($\times 10^{15}$)	Slope	Intercept ($\times 10^{15}$)	r^2	Mean Bias ($\times 10^{15}$)
ATom-1	1.24±0.11	-1.26±0.41	0.84±0.06	-0.34±0.78	1.33±0.10	-1.54±0.39	0.85±0.06	-0.32±0.84	0.99±0.12	-0.86±0.45	0.77±0.10	-0.89±0.91
ATom-2	0.93±0.07	-0.49±0.27	0.85±0.07	-0.74±0.85	1.09±0.07	-1.11±0.24	0.89±0.06	-0.81±0.78	0.75±0.09	-1.20±0.31	0.78±0.09	-2.05±1.08
ATom-3	0.92±0.08	-0.79±0.33	0.81±0.08	-1.09±0.80	1.27±0.10	-2.14±0.39	0.83±0.07	-1.12±0.87	1.28±0.14	-2.37±0.54	0.77±0.09	-1.30±1.04
ATom-4	0.96±0.11	-0.53±0.38	0.79±0.10	-0.65±0.89	1.26±0.10	-1.56±0.34	0.85±0.07	-0.65±0.83	1.09±0.16	-1.61±0.55	0.74±0.11	-1.32±1.11

| all | 1.02±0.05 | -0.79±0.18 | 0.58±0.04 | -0.73±0.87 | 1.24±0.05 | -1.61±0.18 | 0.66±0.03 | -0.76±0.88 | 1.12±0.07 | -1.84±0.27 | 0.42±0.04 | -1.40±1.11 |

The agreement between satellite HCHO retrievals and in situ composite columns is latitude-dependent (Figure 2). Generally, negative bias is smaller near the equator and more pronounced at higher latitudes, although this depends on season (Figure 2). This is probably indicative of issues with latitude-dependent background corrections in satellite retrievals and/or global model bias. A more holistic investigation of relevant models with other ATom observations (e.g., ozone, OH, CO, and other trace gases) may help diagnose the latter. Reactive bromine chemistry at high latitudes may also play a role in the latitude-dependent satellite retrieval bias as bromine oxide (BrO) is a potential interfering absorber at pptv levels with high uncertainty in its concentration distribution. Although the difference between in situ composite columns and satellite retrievals are larger toward high latitudes, in situ composite columns are higher than satellite retrievals even near the equator during ATom-3 (Figure 2). Satellite OMI SAO and OMPS SAO HCHO vertical columns are closer to OMI BIRA during ATom-3 than other seasons (Figure 2). Data on the diurnal variation of HCHO columns in the remote oceanic atmospheric are very limited (e.g., the Mauna Loa site in the supplementary information of Vigouroux et al. (2018)). Given the possible diurnal variation of HCHO, the difference between aircraft sampling time and satellite overpass time (1:30 pm) may account for some, but not the majority, of the discrepancies between satellite and ATom measurements at high latitudes (Fig. 4S and 5S). The differences across latitudes due to time variation may amount to approximately 0.2×10^{15} molecules cm^{-2}, based on the simulation results (Fig. 4S and 5S). Further research is needed to more accurately quantify the diurnal variation of HCHO over oceanic regions. The enhancement of HCHO columns around the -60° latitude bins may be attributed to noise in the OMI BIRA retrievals, specifically anomalous elevated values around filtering gaps when zoomed in, as observed over high southern latitudes in ATom 2 and ATom 3 (Figure 1). Uncertainty-weighted satellite HCHO columns (Eq. (6), all figures in main text) are generally slightly lower than area-weighted satellite HCHO columns (Eq. (7), Figure S6) over the remote oceanic atmosphere, particularly in the OMI BIRA retrieval. However, the different weighting methods do not affect the overall conclusions of the analysis results.

3.3 Differences between retrievals

The three satellite HCHO retrievals all captured the patterns of the enhanced continental outflows though there are some small differences among them. Due to the sensor signal to noise ratio and pixel resolution, OMPS SAO HCHO maps are smoother (less noisy) than OMI HCHO data. OMPS SAO HCHO tends to have higher values near continental outflow regions and lower values far away from the outflow regions than OMI SAO HCHO (Figure 1). Although most of the continental outflows are not captured by the ATom flight tracks that were usually over the remote oceans far away from the continents, OMPS SAO HCHO columns along the ATom flight tracks are still higher than OMI SAO at high values and

334 lower than OMI SAO at lower values (Figure 3). OMI BIRA HCHO columns usually have lower values than the other two retrievals, especially

335 for ATom2.

3.4 Factors contributing to retrieval differences

337 Here we compare each component of satellite retrievals that could contribute to the retrieval differences. First, OMI SAO and OMI BIRA HCHO

338 data are compared to probe the impact of different algorithms on retrievals from the same sensor. Second, OMI SAO and OMPS SAO data are

339 examined to investigate the impact of different sensors on the data with the same retrieval algorithm.
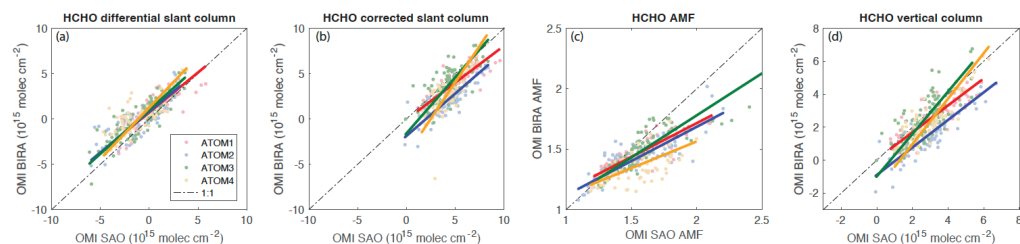
340
341 **Figure 4 Comparison of the (a) HCHO differential slant column, (b) corrected slant column, (c) AMF, and (d) vertical column between OMI BIRA and**
342 **OMI SAO for each ATom deployment.**

343
344
345

Table 3 Parameters for linear fits of OMI BIRA vs OMI SAO retrievals subsampled over ATom flights tracks (see Figure 4).

	OMI BIRA vs OMI SAO															
	Differential slant column				Corrected slant column				AMF				Vertical column			
	Slope	Intercept (×10¹⁵)	r²	Mean Bias (×10¹⁵)	Slope	Intercept (×10¹⁵)	r²	Mean Bias(×10¹⁵)	Slope	Intercept	r²	Mean Bias	Slope	Intercept	r²	Mean Bias(×10¹⁵)
ATom-1	0.88±0.06	0.73±0.12	0.72±0.05	0.66±1.08	0.81±0.07	-0.06±0.37	0.66±0.07	-1.02±1.1	0.55±0.03	0.60±0.05	0.79±0.06	-0.06±0.1	0.82±0.06	0.06±0.22	0.70±0.06	-0.57±0.7
ATom-2	0.90±0.07	0.80±0.14	0.70±0.05	0.87±1.22	0.94±0.08	-1.87±0.36	0.63±0.08	-2.15±1.1	0.58±0.05	0.55±0.07	0.64±0.07	-0.12±0.1	0.84±0.06	-0.90±0.18	0.71±0.06	-1.36±0.7
ATom-3	0.97±0.06	1.00±0.13	0.74±0.04	1.04±1.15	1.23±0.13	-1.59±0.58	0.47±0.07	-0.60±1.3	0.69±0.38	0.39±0.06	0.76±0.05	-0.10±0.1	1.28±0.11	-0.98±0.33	0.56±0.05	-0.20±0.88
ATom-4	1.13±0.14	1.25±0.22	0.45±0.12	1.16±1.6	1.61±0.16	-3.99±0.68	0.57±0.11	-1.43±1.3	0.44±0.06	0.68±0.10	0.37±0.07	-0.16±0.1	1.38±0.13	-1.79±0.39	0.57±0.13	-0.72±0.98

346

3.4.1 OMI SAO vs OMI BIRA

348 Differential HCHO slant column densities of OMI BIRA and OMI SAO are generally well correlated with slopes of 0.8 – 1.1 and intercepts of

349 about 1×10^{15} molecules cm^{-2} (Figure 4a, Table 3). The mean biases of differential HCHO slant column densities of OMI BIRA vs OMI SAO are

350 positive (biased high), also listed in Table 3. Because slant column values are the differential between measured spectra over ocean and the

351 reference sector spectrum, the slant column values go both positive and negative. Differences in differential slant columns may be due to both the

352 retrieval wavelength range and the reference spectrum (Table 1). The strong O_4 absorption at 356.5−359 nm may contribute to the higher

353 differential HCHO slant column in OMI BIRA than OMI SAO; Nowlan et al. (2023) shows that the difference between the two fitting windows

376   is typically $< 4 \times 10^{14}$ molecules cm^{-2} at clean background levels. HCHO absorption cross sections used in the two retrievals come from different

377   sources (see Table 1). The different chosen reference spectra may also contribute to the difference between OMI BIRA and OMI SAO slant

378   columns. The OMI SAO reference spectrum at each across-track position is the average of spectra between 30 ° N to 30 ° S in the orbit with

379   closest in time and an equator crossing closest to 160°W and within 140°–180°W (Nowlan et al., 2023). The OMI BIRA reference spectrum is

380   using the daily average spectrum from the day before for each across-track row in equatorial pacific region (latitude 5° N to 5° S and longitude

381   120°–180° W) (De Smedt et al., 2018).

382

383   Conversion to corrected slant columns generally reduces agreement between the two retrievals (Figure 4b). After slant column corrections, the

384   mean biases of corrected slant columns are negative (biased low) (Table 3). Background HCHO slant columns at slightly different reference

385   sectors and potential other corrections from different models are added so the corrected slant columns are shifted to mostly positive values. The

386   variability in slopes in the two retrievals among different ATom seasons is larger in corrected slant column than in differential slant column,

387   which may be caused by the differences in background HCHO concentrations from different models results. The background HCHO and

388   corrections for OMI SAO and OMPS SAO are from a GEOS-Chem 2018 monthly climatology (Nowlan et al., 2023), while the background

389   HCHO and corrections for OMI BIRA is from the TM5-MP model daily data (De Smedt et al., 2021, 2017).

390

391   Despite the relatively large differences in AMFs, agreement between retrievals for corrected slant columns and vertical columns is relatively

392   similar (Figure 4d). Slopes are similar, and correlation coefficients actually improve by 5-10% with the vertical columns. This is primarily

393   because the low OMI BIRA to OMI SAO AMF ratios correspond to the low HCHO column values and the data are spread. This implies that

394   systematic uncertainties in AMFs are likely minor contributors to overall retrieval error in remote environments. The mean biases in vertical

395   columns are less negative after correlated slant columns normalized by AMF (Table 3).

396   **3.4.2 OMI SAO vs OMPS SAO**

397
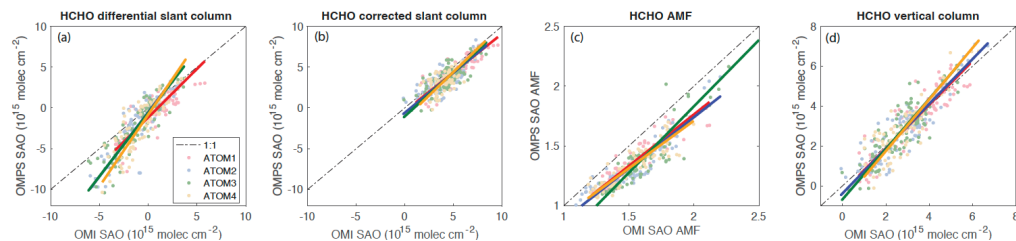
Figure 5. Comparison of the (a) HCHO differential slant column, (b) corrected slant column, (c) AMF, and (d) vertical column between OMPS SAO and OMI SAO for each ATom deployment.

Table 4. Parameters for linear fits of OMPS SAO vs OMI SAO retrievals subsampled over ATom flights tracks (see Figure 5).

	OMI SAO vs OMPS SAO															
	Differential slant column				Corrected slant column				AMF				Vertical column			
	Slope	Intercept ($\times 10^{15}$)	r^2	Mean Bias($\times 10^{15}$)	Slope	Intercept ($\times 10^{15}$)	r^2	Mean Bias ($\times 10^{15}$)	Slope	Intercept	r^2	Mean Bias	Slope	Intercept	r^2	Mean Bias ($\times 10^{15}$)
ATom-1	1.19±0.10	-1.17±0.18	0.65±0.06	-1.06±1.40	0.95±0.07	-0.41±0.35	0.74±0.05	-0.67±0.99	0.86±0.04	0.04±0.06	0.85±0.02	-0.17±0.08	1.09±0.07	-0.31±0.25	0.77±0.04	0.01±0.68
ATom-2	1.58±0.10	-0.52±0.20	0.77±0.06	-0.93±1.75	0.98±0.08	-0.60±0.37	0.63±0.07	-0.68±1.12	0.86±0.04	0.03±0.06	0.84±0.03	-0.19±0.10	1.12±0.06	-0.38±0.19	0.80±0.05	-0.03±0.69
ATom-3	1.55±0.08	-0.62±0.17	0.81±0.02	-1.19±1.61	1.08±0.09	-1.04±0.39	0.61±0.06	-0.70±1.05	1.11±0.04	-0.39±0.07	0.86±0.04	-0.21±0.10	1.26±0.08	-0.68±0.23	0.72±0.05	0.03±0.70
ATom-4	1.76±0.13	-0.82±0.23	0.69±0.05	-1.35±1.84	1.15±0.10	-1.37±0.45	0.61±0.08	-0.72±0.99	0.80±0.05	0.12±0.07	0.80±0.03	-0.19±0.09	1.30±0.08	-0.85±0.24	0.77±0.05	-0.01±0.72

Differential slant columns from OMI SAO and OMPS SAO are generally well correlated (r^2 = 0.65–0.81), with OMPS SAO slant columns lower at low values (Figure 5a). As expected, the mean biases of OMI SAO vs OMPS SAO differential slant columns are negative (Table 4). Different sensor properties and calibrations for the two sensors are likely explanations for these differences. Correction for cross-track pixel dependence sensitivity, HCHO background slant column, and latitude-dependent biases greatly improves agreement, with slopes near 1 for corrected slant columns (Figure 5b) and smaller mean biases (Table 4).

The AMF of OMPS SAO is usually lower than OMI SAO (Figure 5c), with negative mean bias (Table 4). Because the *a priori* gas profiles and scattering weights for OMPS SAO and OMI SAO with the same retrieval algorithms are from the same models, their AMF difference could be due to the different pixel size and the related cloud product, with OMPS SAO using climatology cloud pressure (Nowlan et al., 2023) in scattering weight calculation. The low OMPS SAO to OMI SAO AMF ratios brought the ratios of their vertical columns slightly higher than the ratios of their corrected slant columns and thus smaller mean biases (Table 4). The correlation between OMPS SAO and OMI SAO is improved after normalization by AMF to yield vertical columns, which is similar to the comparison of OMI SAO and OMI BIRA, but the slopes get slightly further from 1.

Although uncertainties in AMFs are likely minor contributors to overall retrieval error in remote ocean environments, roles of *a priori* profiles and scattering weights in contributing to the differences in AMF among the three retrievals are explored. Shape factors (S), scattering weights (SW), AMF density (S×SW×10^6), and AMF accumulative density function for season average are shown in Figure 6. To better visualize the profiles, shape factors only below 15 km are shown in Figure 6, although ATom shape factors are available in altitudes up to ~10 km and satellite shape factors are up to 40 km. The average shape factors of OMI SAO and OMPS SAO are identical due to the same chemical transport model outputs GEOS-Chem 2018 monthly climatology 0.5º × 0.5º data used. OMI BIRA shape factors are close to SAO shape factors except for ATom-2, where OMI BIRA has higher HCHO values near the surface. To be noted, OMI BIRA HCHO is significantly lower than the other two retrievals during ATom-2 (Figure 2). ATom shape factors tend to have lower distribution near the surface than satellite shape factors. The

430 convolution of averaging kernels in satellite HCHO retrievals with ATom measurements was not performed for three reasons: 1) AMFs are likely

431 minor contributors to overall retrieval error in the study regions, 2) In the remote oceanic atmosphere, the shape factors for three retrievals are

432 generally very similar (Figure 6a). Adjusting them to match ATom measurements could systematically alter the AMF of the retrievals but it

433 would not significantly affect the differences among them. 3) HCHO level distributions or shape factors above 10 km are not available from

434 ATom measurements, potentially introducing additional uncertainties in the clean oceanic atmosphere due to high scattering weights (or

435 averaging kernels) at high altitudes. OMI SAO and OMPS SAO scattering weights come from the same radiative transfer model VLIDORT v2.8

436 while scattering weights of OMI BIRA come from VLIDORT v2.7. However, OMPS SAO uses a different cloud product for the scattering

437 weights calculation. The climatology cloud data OMPS SAO uses are fixed at the same height all the time for a given location, giving OMPS

438 SAO the characteristic bump feature near 2 km and leading to the difference in AMF density distribution with OMI SAO and OMI BIRA having

439 one peak along altitude axis at ~ 3 km and OMPS SAO having a peak at higher altitude (~ 4 km). AMF density distribution profiles using ATom

440 *a priori* profiles show similar maximum altitudes to the OMI satellite data. Due to the order of calculations, AMFs estimated from average *a*

441 *priori* and scattering weight of OMI BIRA are not always smaller than that of OMI SAO as shown in Figure 4c. Three satellite retrievals all show

442 that about 10% of AMF density distribution is above 10 km, which was not measured by ATom observations.
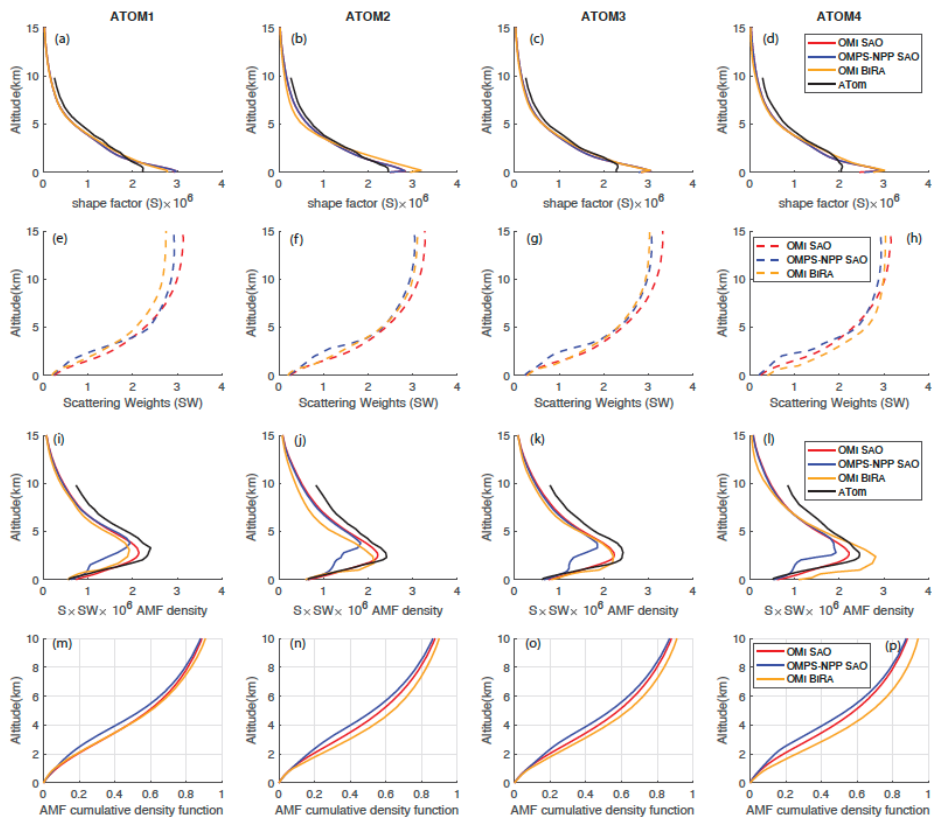
443
444
445 Figure 6. Air mass factor (AMF) components shape factor (S) (a-d), scattering weights (SW) (e-h), and the product of S and SW (S× SW) defined as AMF
446 density (i-l) and the AMF cumulative density function (m-p) for the three satellite retrievals (red: OMI-SAO, blue: OMPS-NPP SAO, orange: OMI BIRA, black:
447 derived from ATom measurements) and four seasons (different columns). ATom shape factor S comes from ATom in situ profiles.
448

449 **4. Conclusions**

450 We use in situ HCHO measurements from four seasonal deployments of the NASA ATom airborne mission to evaluate three satellite retrievals

451 (OMI-SAO (v004), OMPS-NPP SAO, and OMI-BIRA) of total HCHO columns. All retrievals correlate with in situ composite columns over the

452 remote marine regions, with OMI-SAO retrieval exhibiting the best agreement. The mean bias for OMI SAO, OMPS SAO, and OMI BIRA is

453 0.73 ($\pm$0.87) $\times$ 10^{15} molec cm^{-2}, -0.76 ($\pm$0.88) $\times$ 10^{15} molec cm^{-2}, and -1.40 ($\pm$1.11) $\times$ 10^{15} molec cm^{-2}, respectively. Retrievals also capture the

454 patterns of zonal gradients and seasonal variability, with the best agreement near the equator and persistent negative bias at higher latitudes. OMI

455 BIRA HCHO is consistently lower than the other two retrievals, with anomalously low HCHO in February 2017. The discovery of latitude-

456 dependent biases provides useful information for future improvement of satellite HCHO retrievals.

457

458 Intercomparison of results from intermediate retrieval steps reveals the influence of different algorithms and different sensors on derived HCHO

459 columns. Notably, 1) OMI BIRA and SAO differences seem to be mainly due to the applied background corrections, 2) OMI and OMPS have

460 different differential SCDs but corrections fix most of that though OMPS is still slightly higher at high values and lower at low values than OMI,

461 and 3) AMFs can be significantly different, but they don't seem to affect agreement between retrievals because the dynamic range of AMFs is

462 relatively small.

463

464 Evaluation of retrievals using in situ composite columns implies that 1) retrievals of HCHO in remote regions do contain actual measurement

465 information, but models also affect retrieval accuracy; 2) retrievals may be sufficient as inputs to parameterize OH or other species not directly

466 measured from space, but the potential latitude-dependent systematic bias of up to 2×10^{15} molecules cm^{-2}, which is substantial in the remote

467 marine regions, should be considered; 3) this study considered one species in a relatively simple region of the atmosphere, and retrieval

468 differences will vary by molecule and by location. Vertical profiles from in situ instruments are clearly crucial for providing ground truth needed

469 to validate satellite retrievals.

470 **Data availability**

471 The NASA ATom data are available at DAAC archive (https://doi.org/10.3334/ORNLDAAC/1925). OMI SAO v004 data are available at

472 Harvard SAO server (https://waps.cfa.harvard.edu/sao_atmos/data/omi_hcho/). OMPS SAO data are available at NASA GES DISC archive

473 (https://doi.org/10.5067/IIM1GHT07QA8). The OMI BIRA data are available at temis Website (https://www.temis.nl/qa4ecv/hcho.html;

474 https://doi.org/10.18758/71021031).

476

Author contributions

GMW initiated and guided the project. AEK searched for the best satellite datasets to use, contacted satellite people to get the satellite dataset, and used codes from JL to process some satellite data. JL wrote codes to grid and process the satellite datasets and used codes from GMW to calculate in situ composite column. JL re-processed and analyzed the data and discussed the results with GMW and JN. JL wrote the manuscript. GMW, JMSC, and TFH collected ATom ISAF data. GGA, CRN, ZA and IDS provided satellite data. GGA provided the key equation to grid the satellite data. CRN provided additional useful information for the satellite retrievals. ECA and RSH collected ATom TOGA data. All authors reviewed and/or commented on the manuscript.

Competing interests

At least one of the (co-)authors is a member of the editorial board of Atmospheric Measurement Techniques.

Acknowledgments

JL, GMW, AEK, JN, JMSC, and TFH are supported by NASA Tropospheric Composition Program (TCP). JL, AEK, JN, and JMSC are also supported by NOAA Atmospheric Chemistry, Carbon Cycle and Climate (AC4) program (NA19OAR4310164). GGA, CRN and ZA are supported by NASA Making Earth System Data Records for Use in Research Environments (80NSSC18M0091), algorithm maintenance for SAO standard OMI products (80NSSC21K0177), and Algorithm maintenance for SAO OMI products (80NSSC24K0120). GGA and CRN are also supported by NASA Science of Terra, Aqua, and Suomi-NPP (80NSSC18K0691). ECA and RSH are supported by the NSF National Center for Atmospheric Research, which is a major facility sponsored by the U.S. National Science Foundation under Cooperative Agreement No. 1852977.

493

References

Apel, E. C., Hills, A. J., Lueb, R., Zindel, S., Eisele, S., and Riemer, D. D.: A fast-GC/MS system to measure C_2 to C_4 carbonyls and methanol aboard aircraft, Journal of Geophysical Research: Atmospheres, 108, 2002JD003199, https://doi.org/10.1029/2002JD003199, 2003.

Apel, E. C., Hornbrook, R. S., Hills, A. J., Blake, N. J., Barth, M. C., Weinheimer, A., Cantrell, C., Rutledge, S. A., Basarab, B., Crawford, J., Diskin, G., Homeyer, C. R., Campos, T., Flocke, F., Fried, A., Blake, D. R., Brune, W., Pollack, I., Peischl, J., Ryerson, T., Wennberg, P. O.,

Crounse, J. D., Wisthaler, A., Mikoviny, T., Huey, G., Heikes, B., O'Sullivan, D., and Riemer, D. D.: Upper tropospheric ozone production from lightning NO $_x$ -impacted convection: Smoke ingestion case study from the DC3 campaign, Journal of Geophysical Research: Atmospheres, 120, 2505–2523, https://doi.org/10.1002/2014JD022121, 2015.

Baublitz, C. B., Fiore, A. M., Ludwig, S. M., Nicely, J. M., Wolfe, G. M., Murray, L. T., Commane, R., Prather, M. J., Anderson, D. C., Correa, G., Duncan, B. N., Follette-Cook, M., Westervelt, D. M., Bourgeois, I., Brune, W. H., Bui, T. P., DiGangi, J. P., Diskin, G. S., Hall, S. R., McKain, K., Miller, D. O., Peischl, J., Thames, A. B., Thompson, C. R., Ullmann, K., and Wofsy, S. C.: An observation-based, reduced-form model for oxidation in the remote marine troposphere, Proc. Natl. Acad. Sci. U.S.A., 120, e2209735120, https://doi.org/10.1073/pnas.2209735120, 2023.

Brune, W. H., Miller, D. O., Thames, A. B., Allen, H. M., Apel, E. C., Blake, D. R., Bui, T. P., Commane, R., Crounse, J. D., Daube, B. C., Diskin, G. S., DiGangi, J. P., Elkins, J. W., Hall, S. R., Hanisco, T. F., Hannun, R. A., Hintsa, E. J., Hornbrook, R. S., Kim, M. J., McKain, K., Moore, F. L., Neuman, J. A., Nicely, J. M., Peischl, J., Ryerson, T. B., St. Clair, J. M., Sweeney, C., Teng, A. P., Thompson, C., Ullmann, K., Veres, P. R., Wennberg, P. O., and Wolfe, G. M.: Exploring Oxidation in the Remote Free Troposphere: Insights From Atmospheric Tomography (ATom), Journal of Geophysical Research: Atmospheres, 125, e2019JD031685, https://doi.org/10.1029/2019JD031685, 2020.

Cazorla, M., Wolfe, G. M., Bailey, S. A., Swanson, A. K., Arkinson, H. L., and Hanisco, T. F.: A new airborne laser-induced fluorescence instrument for in situ detection of formaldehyde throughout the troposphere and lower stratosphere, Atmos. Meas. Tech., 8, 541–552, https://doi.org/10.5194/amt-8-541-2015, 2015.

Chance, K.: Ultraviolet and visible spectroscopy and spaceborne remote sensing of the Earth's atmosphere, Comptes Rendus Physique, 6, 836–847, https://doi.org/10.1016/j.crhy.2005.07.010, 2005.

Chance, K. and Orphal, J.: Revised ultraviolet absorption cross sections of H2CO for the HITRAN database, Journal of Quantitative Spectroscopy and Radiative Transfer, 112, 1509–1510, https://doi.org/10.1016/j.jqsrt.2011.02.002, 2011.

Chance, K., Palmer, P. I., Spurr, R. J. D., Martin, R. V., Kurosu, T. P., and Jacob, D. J.: Satellite observations of formaldehyde over North America from GOME, Geophysical Research Letters, 27, 3461–3464, https://doi.org/10.1029/2000GL011857, 2000.

Chance, K., Liu, X., Miller, C. C., González Abad, G., Huang, G., Nowlan, C., Souri, A., Suleiman, R., Sun, K., Wang, H., Zhu, L., Zoogman, P., Al-Saadi, J., Antuña-Marrero, J.-C., Carr, J., Chatfield, R., Chin, M., Cohen, R., Edwards, D., Fishman, J., Flittner, D., Geddes, J., Grutter, M., Herman, J. R., Jacob, D. J., Janz, S., Joiner, J., Kim, J., Krotkov, N. A., Lefer, B., Martin, R. V., Mayol-Bracero, O. L., Naeger, A., Newchurch, M., Pfister, G. G., Pickering, K., Pierce, R. B., Rivera Cárdenas, C., Saiz-Lopez, A., Simpson, W., Spinei, E., Spurr, R. J. D., Szykman, J. J., Torres, O., and Wang, J.: TEMPO Green Paper: Chemistry, physics, and meteorology experiments with the Tropospheric Emissions: monitoring of pollution instrument, in: Sensors, Systems, and Next-Generation Satellites XXIII, Sensors, Systems, and Next-Generation Satellites XXIII, Strasbourg, France, 10, https://doi.org/10.1117/12.2534883, 2019.

Chance, K. V., Spurr, R. J. D., Kurosu, T. P., Palmer, P. I., Martin, R. V., Fiore, A., Li, Q., and Jacob, D. J.: Tropospheric formaldehyde measurements from the ESA GOME instrument, Second International Asia-Pacific Symposium on Remote Sensing of the Atmosphere, Environment, and Space, Sendai, Japan, 1–9, https://doi.org/10.1117/12.416945, 2001.

De Smedt, I., Müller, J.-F., Stavrakou, T., Van Der A, R., Eskes, H., and Van Roozendael, M.: Twelve years of global observations of formaldehyde in the troposphere using GOME and SCIAMACHY sensors, Atmos. Chem. Phys., 8, 4947–4963, https://doi.org/10.5194/acp-8-4947-2008, 2008.

De Smedt, I., Van Roozendael, M., Stavrakou, T., Müller, J.-F., Lerot, C., Theys, N., Valks, P., Hao, N., and Van Der A, R.: Improved retrieval of global tropospheric formaldehyde columns from GOME-2/MetOp-A addressing noise reduction and instrumental degradation issues, Atmos. Meas. Tech., 5, 2933–2949, https://doi.org/10.5194/amt-5-2933-2012, 2012.

De Smedt, I., Stavrakou, T., Hendrick, F., Danckaert, T., Vlemmix, T., Pinardi, G., Theys, N., Lerot, C., Gielen, C., Vigouroux, C., Hermans, C., Fayt, C., Veefkind, P., Müller, J.-F., and Van Roozendael, M.: Diurnal, seasonal and long-term variations of global formaldehyde columns inferred from combined OMI and GOME-2 observations, Atmos. Chem. Phys., 15, 12519–12545, https://doi.org/10.5194/acp-15-12519-2015, 2015.

De Smedt, I., van Geffen, J., Richter, A., Beirle, S., Yu, H., Vlietinck, J., Van Roozendael, M., van der A, R., Lorente, A., Scanlon, T., Compernolle, S., Wagner, T., Eskes, H., and Boersma, F.: OMI QA4ECV Product User Guide for HCHO (Version 1.0), 2017.

De Smedt, I., Theys, N., Yu, H., Danckaert, T., Lerot, C., Compernolle, S., Van Roozendael, M., Richter, A., Hilboll, A., Peters, E., Pedergnana, M., Loyola, D., Beirle, S., Wagner, T., Eskes, H., Van Geffen, J., Boersma, K. F., and Veefkind, P.: Algorithm theoretical baseline for formaldehyde retrievals from S5P TROPOMI and from the QA4ECV project, Atmos. Meas. Tech., 11, 2395–2426, https://doi.org/10.5194/amt-11-2395-2018, 2018.

De Smedt, I., Pinardi, G., Vigouroux, C., Compernolle, S., Bais, A., Benavent, N., Boersma, F., Chan, K.-L., Donner, S., Eichmann, K.-U., Hedelt, P., Hendrick, F., Irie, H., Kumar, V., Lambert, J.-C., Langerock, B., Lerot, C., Liu, C., Loyola, D., Piters, A., Richter, A., Rivera Cárdenas, C., Romahn, F., Ryan, R. G., Sinha, V., Theys, N., Vlietinck, J., Wagner, T., Wang, T., Yu, H., and Van Roozendael, M.: Comparative assessment of TROPOMI and OMI formaldehyde observations and validation against MAX-DOAS network column measurements, Atmos. Chem. Phys., 21, 12561–12593, https://doi.org/10.5194/acp-21-12561-2021, 2021.

Fortems-Cheiney, A., Chevallier, F., Pison, I., Bousquet, P., Saunois, M., Szopa, S., Cressot, C., Kurosu, T. P., Chance, K., and Fried, A.: The formaldehyde budget as seen by a global-scale multi-constraint and multi-species inversion system, Atmos. Chem. Phys., 12, 6699–6721, https://doi.org/10.5194/acp-12-6699-2012, 2012.

Franco, B., Marais, E. A., Bovy, B., Bader, W., Lejeune, B., Roland, G., Servais, C., and Mahieu, E.: Diurnal cycle and multi-decadal trend of formaldehyde in the remote atmosphere near 46° N, Atmos. Chem. Phys., 16, 4171–4189, https://doi.org/10.5194/acp-16-4171-2016, 2016.

Goldberg, D. L., Lamsal, L. N., Loughner, C. P., Swartz, W. H., Lu, Z., and Streets, D. G.: A high-resolution and observationally constrained OMI NO$_2$ satellite retrieval, Atmos. Chem. Phys., 17, 11403–11421, https://doi.org/10.5194/acp-17-11403-2017, 2017.

González Abad, G., Liu, X., Chance, K., Wang, H., Kurosu, T. P., and Suleiman, R.: Updated Smithsonian Astrophysical Observatory Ozone Monitoring Instrument (SAO OMI) formaldehyde retrieval, Atmos. Meas. Tech., 8, 19–32, https://doi.org/10.5194/amt-8-19-2015, 2015.

González Abad, G., Vasilkov, A., Seftor, C., Liu, X., and Chance, K.: Smithsonian Astrophysical Observatory Ozone Mapping and Profiler Suite(SAO OMPS) formaldehyde retrieval, Atmos. Meas. Tech., 9, 2797–2812, https://doi.org/10.5194/amt-9-2797-2016, 2016.

563   Guenther, A., Hewitt, C. N., Erickson, D., Fall, R., Geron, C., Graedel, T., Harley, P., Klinger, L., Lerdau, M., Mckay, W. A., Pierce, T., Scholes,
564   B., Steinbrecher, R., Tallamraju, R., Taylor, J., and Zimmerman, P.: A global model of natural volatile organic compound emissions, Journal of
565   Geophysical Research: Atmospheres, 100, 8873–8892, https://doi.org/10.1029/94JD02950, 1995.

566   Gulde, S. T., Kolm, M. G., Maurer, R., Sallusti, M., Bagnasco, G., Smith, D. J., and Bazalgette Courrèges-Lacoste, G.: Sentinel 4: a geostationary
567   imaging UVN spectrometer for air quality monitoring: status of design, performance and development, in: International Conference on Space
568   Optics — ICSO 2014, International Conference on Space Optics 2014, Tenerife, Canary Islands, Spain, 39, https://doi.org/10.1117/12.2304099,
569   2017.

570   Herman, J., Cede, A., Spinei, E., Mount, G., Tzortziou, M., and Abuhassan, N.: NO_2 column amounts from ground-based Pandora and MFDOAS
571   spectrometers using the direct-sun DOAS technique: Intercomparisons and application to OMI validation, Journal of Geophysical Research:
572   Atmospheres, 114, 2009JD011848, https://doi.org/10.1029/2009JD011848, 2009.

573   Kim, J., Jeong, U., Ahn, M.-H., Kim, J. H., Park, R. J., Lee, H., Song, C. H., Choi, Y.-S., Lee, K.-H., Yoo, J.-M., Jeong, M.-J., Park, S. K., Lee,
574   K.-M., Song, C.-K., Kim, S.-W., Kim, Y. J., Kim, S.-W., Kim, M., Go, S., Liu, X., Chance, K., Chan Miller, C., Al-Saadi, J., Veihelmann, B.,
575   Bhartia, P. K., Torres, O., Abad, G. G., Haffner, D. P., Ko, D. H., Lee, S. H., Woo, J.-H., Chong, H., Park, S. S., Nicks, D., Choi, W. J., Moon,
576   K.-J., Cho, A., Yoon, J., Kim, S., Hong, H., Lee, K., Lee, H., Lee, S., Choi, M., Veefkind, P., Levelt, P. F., Edwards, D. P., Kang, M., Eo, M.,
577   Bak, J., Baek, K., Kwon, H.-A., Yang, J., Park, J., Han, K. M., Kim, B.-R., Shin, H.-W., Choi, H., Lee, E., Chong, J., Cha, Y., Koo, J.-H., Irie, H.,
578   Hayashida, S., Kasai, Y., Kanaya, Y., Liu, C., Lin, J., Crawford, J. H., Carmichael, G. R., Newchurch, M. J., Lefer, B. L., Herman, J. R., Swap,
579   R. J., Lau, A. K. H., Kurosu, T. P., Jaross, G., Ahlers, B., Dobber, M., McElroy, C. T., and Choi, Y.: New Era of Air Quality Monitoring from
580   Space: Geostationary Environment Monitoring Spectrometer (GEMS), Bulletin of the American Meteorological Society, 101, E1–E22,
581   https://doi.org/10.1175/BAMS-D-18-0013.1, 2020.

582   Kwon, H. -A., Abad, G. G., Nowlan, C. R., Chong, H., Souri, A. H., Vigouroux, C., Röhling, A., Kivi, R., Makarova, M., Notholt, J., Palm, M.,
583   Winkler, H., Té, Y., Sussmann, R., Rettinger, M., Mahieu, E., Strong, K., Lutsch, E., Yamanouchi, S., Nagahama, T., Hannigan, J. W., Zhou, M.,
584   Murata, I., Grutter, M., Stremme, W., De Mazière, M., Jones, N., Smale, D., and Morino, I.: Validation of OMPS Suomi NPP and OMPS NOAA-
585   20 Formaldehyde Total Columns With NDACC FTIR Observations, Earth and Space Science, 10, e2022EA002778,
586   https://doi.org/10.1029/2022EA002778, 2023.

587   Kwon, H.-A., Park, R. J., González Abad, G., Chance, K., Kurosu, T. P., Kim, J., De Smedt, I., Van Roozendael, M., Peters, E., and Burrows, J.:
588   Description of a formaldehyde retrieval algorithm for the Geostationary Environment Monitoring Spectrometer (GEMS), Atmos. Meas. Tech.,
589   12, 3551–3571, https://doi.org/10.5194/amt-12-3551-2019, 2019.

590   Li, C., Joiner, J., Krotkov, N. A., and Dunlap, L.: A new method for global retrievals of HCHO total columns from the Suomi National Polar-
591   orbiting Partnership Ozone Mapping and Profiler Suite, Geophysical Research Letters, 42, 2515–2522, https://doi.org/10.1002/2015GL063204,
592   2015.

593   Millet, D. B., Jacob, D. J., Turquety, S., Hudman, R. C., Wu, S., Fried, A., Walega, J., Heikes, B. G., Blake, D. R., Singh, H. B., Anderson, B. E.,
594   and Clarke, A. D.: Formaldehyde distribution over North America: Implications for satellite retrievals of formaldehyde columns and isoprene
595   emission, Journal of Geophysical Research: Atmospheres, 111, 2005JD006853, https://doi.org/10.1029/2005JD006853, 2006.

596 Novak, G. A. and Bertram, T. H.: Reactive VOC Production from Photochemical and Heterogeneous Reactions Occurring at the Air–Ocean
597 Interface, Acc. Chem. Res., 53, 1014–1023, https://doi.org/10.1021/acs.accounts.0c00095, 2020.

598 Nowlan, C. and Gonzalez Abad, G.: README Document for OMPS_NPP_NMHCHO_L2 and OMPS_N20_NMHCHO_L2, 2022.

599 Nowlan, C. R., González Abad, G., Kwon, H., Ayazpour, Z., Chan Miller, C., Chance, K., Chong, H., Liu, X., O'Sullivan, E., Wang, H., Zhu, L.,
600 De Smedt, I., Jaross, G., Seftor, C., and Sun, K.: Global Formaldehyde Products From the Ozone Mapping and Profiler Suite (OMPS) Nadir
601 Mappers on Suomi NPP and NOAA-20, Earth and Space Science, 10, e2022EA002643, https://doi.org/10.1029/2022EA002643, 2023.

602 Prather, M. J., Zhu, X., Flynn, C. M., Strode, S. A., Rodriguez, J. M., Steenrod, S. D., Liu, J., Lamarque, J.-F., Fiore, A. M., Horowitz, L. W.,
603 Mao, J., Murray, L. T., Shindell, D. T., and Wofsy, S. C.: Global atmospheric chemistry – which air matters, Atmos. Chem. Phys., 17, 9081–
604 9102, https://doi.org/10.5194/acp-17-9081-2017, 2017.

605 Singh, H. B., Salas, L. J., Chatfield, R. B., Czech, E., Fried, A., Walega, J., Evans, M. J., Field, B. D., Jacob, D. J., Blake, D., Heikes, B., Talbot,
606 R., Sachse, G., Crawford, J. H., Avery, M. A., Sandholm, S., and Fuelberg, H.: Analysis of the atmospheric distribution, sources, and sinks of
607 oxygenated volatile organic chemicals based on measurements over the Pacific during TRACE-P, Journal of Geophysical Research:
608 Atmospheres, 109, 2003JD003883, https://doi.org/10.1029/2003JD003883, 2004.

609 Spurr, R. J. D.: VLIDORT: A linearized pseudo-spherical vector discrete ordinate radiative transfer code for forward model and retrieval studies
610 in multilayer multiple scattering media, Journal of Quantitative Spectroscopy and Radiative Transfer, 102, 316–342,
611 https://doi.org/10.1016/j.jqsrt.2006.05.005, 2006.

612 Thomas, W., Hegels, E., Meisner, R., Slijkhuis, S., Spurr, R., and Chance, K.: Detection of trace species in the troposphere using backscatter
613 spectra obtained by the GOME spectrometer, in: IGARSS '98. Sensing and Managing the Environment. 1998 IEEE International Geoscience and
614 Remote Sensing. Symposium Proceedings. (Cat. No.98CH36174), IGARSS '98. Sensing and Managing the Environment. 1998 IEEE
615 International Geoscience and Remote Sensing. Symposium Proceedings. (Cat. No.98CH36174), Seattle, WA, USA, 2612–2614 vol.5,
616 https://doi.org/10.1109/IGARSS.1998.702295, 1998.

617 Thompson, C. R., Wofsy, S. C., Prather, M. J., Newman, P. A., Hanisco, T. F., Ryerson, T. B., Fahey, D. W., Apel, E. C., Brock, C. A., Brune,
618 W. H., Froyd, K., Katich, J. M., Nicely, J. M., Peischl, J., Ray, E., Veres, P. R., Wang, S., Allen, H. M., Asher, E., Bian, H., Blake, D., Bourgeois,
619 I., Budney, J., Bui, T. P., Butler, A., Campuzano-Jost, P., Chang, C., Chin, M., Commane, R., Correa, G., Crounse, J. D., Daube, B., Dibb, J. E.,
620 DiGangi, J. P., Diskin, G. S., Dollner, M., Elkins, J. W., Fiore, A. M., Flynn, C. M., Guo, H., Hall, S. R., Hannun, R. A., Hills, A., Hintsa, E. J.,
621 Hodzic, A., Hornbrook, R. S., Huey, L. G., Jimenez, J. L., Keeling, R. F., Kim, M. J., Kupc, A., Lacey, F., Lait, L. R., Lamarque, J.-F., Liu, J.,
622 McKain, K., Meinardi, S., Miller, D. O., Montzka, S. A., Moore, F. L., Morgan, E. J., Murphy, D. M., Murray, L. T., Nault, B. A., Neuman, J. A.,
623 Nguyen, L., Gonzalez, Y., Rollins, A., Rosenlof, K., Sargent, M., Schill, G., Schwarz, J. P., Clair, J. M. St., Steenrod, S. D., Stephens, B. B.,
624 Strahan, S. E., Strode, S. A., Sweeney, C., Thames, A. B., Ullmann, K., Wagner, N., Weber, R., Weinzierl, B., Wennberg, P. O., Williamson, C.
625 J., Wolfe, G. M., and Zeng, L.: The NASA Atmospheric Tomography (ATom) Mission: Imaging the Chemistry of the Global Atmosphere,
626 Bulletin of the American Meteorological Society, 103, E761–E790, https://doi.org/10.1175/BAMS-D-20-0315.1, 2022.

627 Vigouroux, C., Bauer Aquino, C. A., Bauwens, M., Becker, C., Blumenstock, T., De Mazière, M., García, O., Grutter, M., Guarin, C., Hannigan,
628 J., Hase, F., Jones, N., Kivi, R., Koshelev, D., Langerock, B., Lutsch, E., Makarova, M., Metzger, J.-M., Müller, J.-F., Notholt, J., Ortega, I.,
629 Palm, M., Paton-Walsh, C., Poberovskii, A., Rettinger, M., Robinson, J., Smale, D., Stavrakou, T., Stremme, W., Strong, K., Sussmann, R., Té,

630 Y., and Toon, G.: NDACC harmonized formaldehyde time series from 21 FTIR stations covering a wide range of column abundances, Atmos.
631 Meas. Tech., 11, 5049–5073, https://doi.org/10.5194/amt-11-5049-2018, 2018.

632 Vigouroux, C., Langerock, B., Bauer Aquino, C. A., Blumenstock, T., Cheng, Z., De Mazière, M., De Smedt, I., Grutter, M., Hannigan, J. W.,
633 Jones, N., Kivi, R., Loyola, D., Lutsch, E., Mahieu, E., Makarova, M., Metzger, J.-M., Morino, I., Murata, I., Nagahama, T., Notholt, J., Ortega,
634 I., Palm, M., Pinardi, G., Röhling, A., Smale, D., Stremme, W., Strong, K., Sussmann, R., Té, Y., Van Roozendael, M., Wang, P., and Winkler,
635 H.: TROPOMI–Sentinel-5 Precursor formaldehyde validation using an extensive network of ground-based Fourier-transform infrared stations,
636 Atmos. Meas. Tech., 13, 3751–3767, https://doi.org/10.5194/amt-13-3751-2020, 2020.

637 Wang, Y., Beirle, S., Lampel, J., Koukouli, M., De Smedt, I., Theys, N., Li, A., Wu, D., Xie, P., Liu, C., Van Roozendael, M., Stavrakou, T.,
638 Müller, J.-F., and Wagner, T.: Validation of OMI, GOME-2A and GOME-2B tropospheric NO$_2$,
639 SO$_2$ and HCHO products using MAX-DOAS observations from 2011 to 2014 in Wuxi, China: investigation of the
640 effects of priori profiles and aerosols on the satellite products, Atmos. Chem. Phys., 17, 5007–5033, https://doi.org/10.5194/acp-17-5007-2017,
641 2017.

642 Wolfe, G. M., Nicely, J. M., St. Clair, J. M., Hanisco, T. F., Liao, J., Oman, L. D., Brune, W. B., Miller, D., Thames, A., González Abad, G.,
643 Ryerson, T. B., Thompson, C. R., Peischl, J., McKain, K., Sweeney, C., Wennberg, P. O., Kim, M., Crounse, J. D., Hall, S. R., Ullmann, K.,
644 Diskin, G., Bui, P., Chang, C., and Dean-Day, J.: Mapping hydroxyl variability throughout the global remote troposphere via synthesis of
645 airborne and satellite formaldehyde observations, Proc. Natl. Acad. Sci. U.S.A., 116, 11171–11180, https://doi.org/10.1073/pnas.1821661116,
646 2019.

647 Zara, M., Boersma, K. F., De Smedt, I., Richter, A., Peters, E., Van Geffen, J. H. G. M., Beirle, S., Wagner, T., Van Roozendael, M., Marchenko,
648 S., Lamsal, L. N., and Eskes, H. J.: Improved slant column density retrieval of nitrogen dioxide and formaldehyde for OMI and GOME-2A from
649 QA4ECV: intercomparison, uncertainty characterisation, and trends, Atmos. Meas. Tech., 11, 4033–4058, https://doi.org/10.5194/amt-11-4033-
650 2018, 2018.

651 Zhu, L., Jacob, D. J., Kim, P. S., Fisher, J. A., Yu, K., Travis, K. R., Mickley, L. J., Yantosca, R. M., Sulprizio, M. P., De Smedt, I., Gonzalez
652 Abad, G., Chance, K., Li, C., Ferrare, R., Fried, A., Hair, J. W., Hanisco, T. F., Richter, D., Scarino, A. J., Walega, J., Weibring, P., and Wolfe,
653 G. M.: Observing atmospheric formaldehyde (HCHO) from space: validation and intercomparison of six retrievals from four satellites (OMI,
654 GOME2A, GOME2B, OMPS) with SEAC^{4}RS aircraft observations over the Southeast US, Gases/Remote
655 Sensing/Troposphere/Chemistry (chemical composition and reactions), https://doi.org/10.5194/acp-2016-162, 2016.

656 Zhu, L., González Abad, G., Nowlan, C. R., Chan Miller, C., Chance, K., Apel, E. C., DiGangi, J. P., Fried, A., Hanisco, T. F., Hornbrook, R. S.,
657 Hu, L., Kaiser, J., Keutsch, F. N., Permar, W., St. Clair, J. M., and Wolfe, G. M.: Validation of satellite formaldehyde (HCHO) retrievals using
658 observations from 12 aircraft campaigns, Atmos. Chem. Phys., 20, 12329–12345, https://doi.org/10.5194/acp-20-12329-2020, 2020.
659
660
661
662
663
664

665
666
667
668
669
670
671
672
673